Delft University of Technology

3-D Contrast Source Inversion-Electrical Properties Tomography

Leijsen, Reijer L.; Brink, Wyger M.; van den Berg, Cornelis A.T.; Webb, Andrew G.; Remis, Rob F.

Important note
To cite this publication, please use the final published version (if applicable).
Please check the document version above.

Three-Dimensional Contrast Source Inversion-Electrical Properties Tomography

Reijer L. Leijsen*, Wyger M. Brink, Cornelis A.T. van den Berg, Andrew G. Webb, and Rob F. Remis

Abstract—Contrast source inversion – electrical properties tomography (CSI-EPT) is an iterative reconstruction method to retrieve the electrical properties (EPs) of tissues from MR data. The method is based on integral representations of the electromagnetic (EM) field and has been shown to allow EP reconstructions of small structures as well as tissue boundaries with compelling accuracy. However, to date CSI-EPT has been implemented for two-dimensional (2D) configurations only which limits its applicability. In this paper, a full three-dimensional (3D) extension of the CSI-EPT method is presented, to enable CSI-EPT to be applied to realistic 3D scenarios. Here, we demonstrate a proof-of-principle of 3D CSI-EPT and present reconstructions of a 3D abdominal body section and a 3D head model using different settings of the transmit coil. Numerical results show that the full 3D approach yields accurate reconstructions of the EPs, even at tissue boundaries and is most accurate in regions where the absolute value of the electric field is highest.

Index Terms—Electrical properties tomography, three-dimensional contrast source inversion, magnetic resonance imaging, electromagnetic Green's tensor field representations.

I. INTRODUCTION

ELECTRICAL properties tomography (EPT) is a non-invasive reconstruction technique to retrieve the tissue-dependent electrical properties (EPs) (conductivity σ and permittivity ε) of biological tissue from magnetic fields generated by radiofrequency (RF) coils in a magnetic resonance imaging (MRI) scanner. The EPs of tissue are of great interest, since these properties contribute to specific absorption rate (SAR) [1], they can be used to aid the discrimination of cancerous tissue from benign tissue [2], and they can also be used for the modeling of electromagnetic (EM) fields that are used in hyperthermia treatment planning [3]. The main benefits of EPT over other EP reconstruction modalities is that it uses the RF fields of an MRI system, which can penetrate biological tissues and it does not make use of surface electrode mounting, current injection, additional hardware or physical rotation of the imaged object [4], [5].

The introduction of what is nowadays called EPT was by Haacke *et al.* in 1991 [6] and the first application of this

method was in 2003 by Wen [7]. In this method, the transmit magnetic field, the B_1^+ field, is used to directly reconstruct the EPs based on local field equations. The introduced homogeneous Helmholtz equation is still very frequently used as a starting point in EPT, since it is fast and easy to implement [1], [8]–[13]. However, in this method a higher order spatial differentiation operator acts on the measurement data. This introduces erroneous behavior around tissue interfaces and makes the method sensitive to noise, leading to long acquisition times to meet the input signal-to-noise ratio requirements. Attempts to improve the boundary artifact by including the spatial gradient of the EPs in the algorithm still suffer from the noise sensitivity [14]–[16], while recent EPT approaches that avoid differentiation of the measurement data lack accuracy near tissue boundaries [17], [18].

Contrast source inversion (CSI)-EPT is a reconstruction method that avoids the assumption of locally homogeneous media by making use of a global integral approach instead of a local differential approach. This makes the method more reliable near tissue boundaries and, due to the smoothing effect of the integrals, less sensitive to noise [19], [20]. To date, however, CSI-EPT has been implemented for two-dimensional E-polarized RF fields only, which assumes longitudinal invariance of both the sources and the object. The RF coil in such a configuration excites E-polarized RF waves characterized by a magnetic field that is purely transverse and an electric field that has a longitudinal component only. This limits the applicability of CSI-EPT in experimental conditions where longitudinal tissue interfaces as well as the finite longitudinal coverage of the RF transmit coil violate these assumptions. The issue is illustrated by Balidemaj et al. [21], where the RF fields present in a 3T system show distinct differences than those obtained in the corresponding 2D model, which would lead to erroneous reconstructions when used as an input to 2D CSI-EPT.

In this paper, we present a three-dimensional implementation of CSI-EPT in which all EM field components are taken into account. Consequently, we work with the global Green's tensor field representations instead of the scalar integral field representations used in the two-dimensional E-polarized case. The basic algorithm used in 2D and 3D are very similar, but the form of the operators are specific to the dimensionality. As the discretization of the 3D operators is obviously more involved, details about the discretization procedure are presented as well as a Kronecker product formulation of the resulting discretized operators, which allows for a straightforward implementation. A 3D volumetric integral equation approach is also presented in [22], using the variational Born iterative

method, but using CSI-EPT has the advantage that it does not have to solve a computationally expensive forward problem at every iteration. Furthermore, we focus on inverting B_1^+ data collected at 3T, since in practice EPT is usually applied at higher field strengths (3T and above). Moreover, we only use volumetric B_1^+ data collected on the body part of interest. We present three-dimensional CSI-EPT reconstructions of the abdomen and head of a female body model. The influence of the magnitude of the electric field strength within the domain of interest on the reconstructions is also studied by comparing different excitation settings. Finally, we present a comparison between two- and three-dimensional CSI-EPT reconstructions using 3D input data with different levels of longitudinal invariance, to demonstrate the relevance of the 3D formulation.

This paper is organized as follows. In Section II we present the basic integral representations of the RF field. The discretization of these representations is discussed in the Appendix. In Section III we briefly review the basic CSI-EPT method, while in Section IV we illustrate the performance of 3D CSI-EPT through a number of numerical experiments using volumetric B_1^+ data collected inside a female body model. Finally, the conclusions and a discussion can be found in Section V.

II. INTEGRAL REPRESENTATIONS OF THE RF FIELD

In this section, we briefly review the basic CSI-EPT integral representations of the electromagnetic field. Our discussion will be brief, since formulating these representations is well documented in the literature (see [23], for example). The discretization of these representations is discussed in the Appendix, where we present a Kronecker product formulation that can be conveniently implemented in Matlab using the `kron` command. We assume that the conductivity and permittivity are isotropic at the Larmor frequency ω, we ignore spatial permeability variations ($\mu = \mu_0$), since they are considered small for biological tissue, and we use the time factor convention $\exp(j\omega t)$, with j the imaginary unit.

Let the antenna (coil) that generates the RF field occupy a bounded source domain and let an object (e.g. a person) that is present inside the MR scanner occupy the bounded object domain $\mathbb{D}^{\text{obj}}$. Both domains are obviously disjoint, since the antenna is not placed inside the object of interest.

The total electromagnetic field $\{\mathbf{E}, \mathbf{H}\}$ that is present in such a configuration is written as a superposition of an incident and a scattered field as

$$\mathbf{E} = \mathbf{E}^{\text{inc}} + \mathbf{E}^{\text{sc}} \quad \text{and} \quad \mathbf{H} = \mathbf{H}^{\text{inc}} + \mathbf{H}^{\text{sc}}, \tag{1}$$

where $\{\mathbf{E}^{\text{inc}}, \mathbf{H}^{\text{inc}}\}$ is the incident electromagnetic field that is present inside the scanner in the absence of the object, and $\{\mathbf{E}^{\text{sc}}, \mathbf{H}^{\text{sc}}\}$ is the scattered field due to the presence of the object. For this scattered field, we have the integral representations

$$\mathbf{E}^{\text{sc}}(\mathbf{x}) = (k_{\text{b}}^2 + \nabla\nabla\cdot)\mathbf{A}(\mathbf{x}) \tag{2}$$

and

$$\mathbf{H}^{\text{sc}}(\mathbf{x}) = \eta_{\text{b}}\nabla \times \mathbf{A}(\mathbf{x}), \tag{3}$$

where $\mathbf{A}$ is the vector potential given by

$$\mathbf{A}(\mathbf{x}) = \int_{\mathbf{x}' \in \mathbb{D}^{\text{obj}}} G(\mathbf{x} - \mathbf{x}')\chi(\mathbf{x}')\mathbf{E}(\mathbf{x}')\,\mathrm{d}V \tag{4}$$

with

$$G(\mathbf{x}) = \frac{\exp(-jk_{\text{b}}|\mathbf{x}|)}{4\pi|\mathbf{x}|}, \quad \mathbf{x} \neq \mathbf{0}, \tag{5}$$

the scalar Green's function of the homogeneous background medium (air) and χ the contrast function defined as

$$\chi(\mathbf{x}) = \frac{\eta(\mathbf{x})}{\eta_{\text{b}}} - 1. \tag{6}$$

In the above equations, $\eta = \sigma + j\omega\varepsilon$ is the per-unit-length admittance of the object, with σ and ε the spatially varying conductivity and permittivity profiles of the object, respectively. Finally, $k_{\text{b}} = \omega/c_0$ is the wavenumber of the background medium and $\eta_{\text{b}} = j\omega\varepsilon_0$ with c_0 and ε_0 the electromagnetic wave speed and permittivity in vacuum, respectively.

By restricting the position vector $\mathbf{x}$ in the integral representations of (2) and (3) to the object domain $\mathbb{D}^{\text{obj}}$, we obtain integral representations of the RF field inside the object of interest. In particular, (3) relates the scattered magnetic field strength to the contrast and electric field strength via the vector potential $\mathbf{A}$, while the electric field strength and the contrast function inside the object have to satisfy (2). Consequently, the field representation of (3) for the x- and y-components of the magnetic field strength can be used to model $B_1^+ = (B_x + jB_y)/2$ data collected inside the body, while (2) serves as a consistency equation that provides a relation between the contrast function and the corresponding electric field strength. Explicitly, by substituting the x- and y-components of the field representation of (3) in the definition of the scattered B_1^+ field, we obtain

$$B_1^{+;\text{sc}}(\mathbf{x}) = \frac{\omega}{c_0^2}\left(\partial^+ A_z - \partial_z A^+\right), \tag{7}$$

where ∂^+ is the so-called del-operator defined as $\partial^+ = \frac{1}{2}(\partial_x + j\partial_y)$, and $A^+ = \frac{1}{2}(A_x + jA_y)$. We observe that the scattered B_1^+ field is given by the difference between transverse variations of the longitudinal component of the vector potential ($\partial^+ A_z$) and longitudinal variations of the transverse A^+ field ($\partial_z A^+$).

To summarize, by restricting $\mathbf{x}$ to $\mathbb{D}^{\text{obj}}$, (7) provides a data model for the scattered B_1^+ field inside the object of interest and even though the contrast χ and the electric field strength $\mathbf{E}$ are unknown, we do know that (2) has to be satisfied as well.

III. 3D CSI-EPT

The CSI method is well described in the literature [24], [25], [26] and we therefore only give a brief discussion of this method in the EPT context.

As a first step, we introduce the contrast source

$$\mathbf{w}(\mathbf{x}) = \chi(\mathbf{x})\mathbf{E}(\mathbf{x}) \tag{8}$$

and use the expression for the total electric field as given in (1) to write the integral representation for the scattered electric field strength as

$$\mathbf{E}(\mathbf{x}) - (k_{\text{b}}^2 + \nabla\nabla\cdot)\mathbf{A}(\mathbf{x}) = \mathbf{E}^{\text{inc}}(\mathbf{x}). \tag{9}$$

Multiplying this equation by the contrast function χ, we obtain the so-called object or state equation

$$\mathbf{w}(\mathbf{x}) - \chi \mathcal{G}_{\mathrm{obj}}\{\mathbf{w}\}(\mathbf{x}) = \chi(\mathbf{x})\mathbf{E}^{\mathrm{inc}}(\mathbf{x}), \qquad (10)$$

where we have introduced the object operator

$$\mathcal{G}_{\mathrm{obj}}\{\mathbf{w}\}(\mathbf{x}) = (k_{\mathrm{b}}^2 + \nabla\nabla\cdot) \int_{\mathbf{x}' \in \mathbb{D}^{\mathrm{obj}}} G(\mathbf{x} - \mathbf{x}')\mathbf{w}(\mathbf{x}')\,\mathrm{d}V. \quad (11)$$

If χ and $\mathbf{w}$ are approximations for the contrast function and the contrast source, respectively, we introduce the residual of the object equation that corresponds to these approximations as

$$\mathbf{r} = \chi \mathbf{E}^{\mathrm{inc}} - \mathbf{w} + \chi \mathcal{G}_{\mathrm{obj}}\{\mathbf{w}\}, \qquad (12)$$

and measure its size through the standard L^2-norm on $\mathbb{D}^{\mathrm{obj}}$ as

$$\|\mathbf{r}\|_{\mathrm{obj}} = \left(\int_{\mathbf{x} \in \mathbb{D}^{\mathrm{obj}}} |\mathbf{r}(\mathbf{x})|^2 \,\mathrm{d}V \right)^{1/2}. \qquad (13)$$

Similarly, by substituting the vector potential of (4) in (7), we obtain the data equation

$$B_1^{+;\mathrm{sc}}(\mathbf{x}) = \mathcal{G}_{\mathrm{data}}\{\mathbf{w}\}(\mathbf{x}), \qquad (14)$$

where we have introduced the data operator

$$\mathcal{G}_{\mathrm{data}}\{\mathbf{w}\}(\mathbf{x}) = \frac{\omega}{c_0^2} \tilde{\nabla} \cdot \int_{\mathbf{x}' \in \mathbb{D}^{\mathrm{obj}}} G(\mathbf{x} - \mathbf{x}')\mathbf{w}(\mathbf{x}')\,\mathrm{d}V \qquad (15)$$

with $\tilde{\nabla} = -\frac{1}{2}(\mathbf{i}_x + \mathbf{j}\mathbf{i}_y)\partial_z + \mathbf{i}_z\partial^+$ and $\{\mathbf{i}_x, \mathbf{i}_y, \mathbf{i}_z\}$ the standard basis for 3D space. If $\mathbf{w}$ is an approximation of the contrast source, then the residual of the data equation that corresponds to this approximation is introduced as

$$\rho = B_1^{+;\mathrm{sc}} - \mathcal{G}_{\mathrm{data}}\{\mathbf{w}\} \qquad (16)$$

and its magnitude is also measured using the L^2-norm on $\mathbb{D}^{\mathrm{obj}}$. Note that the incident B_1^+ field is simulated from the known coil geometry and that subtraction of this field from the measured B_1^+ field gives the $B_1^{+;\mathrm{sc}}$ as presented in (16).

In CSI-EPT, we now introduce the objective function

$$F(\mathbf{w}, \chi) = \frac{\|\mathbf{r}\|_{\mathrm{obj}}^2}{\|\chi \mathbf{E}^{\mathrm{inc}}\|_{\mathrm{obj}}^2} + \frac{\|\rho\|_{\mathrm{obj}}^2}{\|B_1^{+;\mathrm{sc}}\|_{\mathrm{obj}}^2}. \qquad (17)$$

to measure the discrepancy in satisfying the object and data equations and we attempt to find a minimum of this function by constructing a sequence of contrast functions and a sequence of contrast sources that converge to a minimum of the objective function F. Specifically, let $\chi^{[n-1]}$ and $\mathbf{w}^{[n-1]}$ be given approximations of the contrast function and contrast source, respectively. As a first step in CSI-EPT, we keep the contrast function $\chi^{[n-1]}$ fixed and update the contrast source according to the update formula

$$\mathbf{w}^{[n]} = \mathbf{w}^{[n-1]} + \alpha^{[n]}\mathbf{v}^{[n]}, \qquad (18)$$

where $\alpha^{[n]}$ is the step length and $\mathbf{v}^{[n]}$ the update direction. For these update directions, one usually takes Polak-Ribière update directions, but other choices (Fletcher-Reeves, Hesteness-Stiefel) are possible as well [27]. To compute the update directions, the gradient of $F(\mathbf{w}, \chi^{[n-1]})$ with respect to $\mathbf{w}$ is required. Explicit expressions for this gradient and the step length $\alpha^{[n]}$ can be found in [24], for example.

Having updated the contrast source, we subsequently compute the corresponding electric field strength according to (cf. (9))

$$\mathbf{E}^{[n]}(\mathbf{x}) = \mathbf{E}^{\mathrm{inc}}(\mathbf{x}) + \mathcal{G}_{\mathrm{obj}}\{\mathbf{w}^{[n]}\}(\mathbf{x}) \qquad (19)$$

and, finally, update the contrast function using the formula [24]

$$\chi^{[n]} = \frac{\mathbf{w}^{[n]} \cdot \mathbf{E}^{[n];*}}{|\mathbf{E}^{[n]}|^2} \qquad (20)$$

which holds locally at every point in $\mathbb{D}^{\mathrm{obj}}$ and where the asterisk denotes complex conjugation. Note that CSI-EPT attempts to reconstruct the electric field strength (see (19)) and therefore allows SAR estimations as well.

Having found an updated contrast function, the above process can now be repeated and we arrive at the standard CSI-EPT method:

CSI-EPT

- Given an initial contrast function $\chi^{[0]}$ and contrast source $\mathbf{w}^{[0]}$
- For $n = 1, 2, \ldots$
  1) If $F(\mathbf{w}^{[n-1]}, \chi^{[n-1]}) < $ tolerance then stop
  2) Update the contrast source according to (18)
  3) Compute the electric field strength corresponding to the updated contrast source via (19)
  4) Update the contrast function according to (20)

The initial guesses in the above algorithm have to be provided, of course. Many choices are possible and any *a priori* information about the dielectric properties can be included. A general approach that does not take such information into account is to first determine an initial contrast source $\mathbf{w}^{[0]}$ via backprojection [24] and subsequently determine the electric field strength and initial contrast via (19) and (20) with $n = 0$.

By carrying out the above CSI-EPT algorithm, a sequence of the contrast sources and a sequence of contrast functions is generated. These sequences terminate as soon as a predefined tolerance level of the objective function (or a specified number of iterations) is reached. At iteration n, the dielectric tissue parameters can be retrieved from the reconstructed contrast function $\chi^{[n]}$ as

$$\sigma = \mathrm{Re}\left[\left(\chi^{[n]} + 1\right)\eta_{\mathrm{b}}\right] \quad \text{and} \quad \varepsilon = \mathrm{Re}\left[\left(\chi^{[n]} + 1\right)\varepsilon_0\right], \qquad (21)$$

where Re denotes the real part and ε the absolute permittivity, which is related to the relative permittivity via $\varepsilon = \varepsilon_0\varepsilon_{\mathrm{r}}$.

IV. NUMERICAL RESULTS

To test the 3D CSI-EPT algorithm, we reconstruct the dielectric tissue maps of different parts of the female body model Ella from the IT'IS Foundation with an isotropic voxel size of 2.5 mm [28]. In our first 3D simulation, we select a region of 72-by-124-by-41 voxels around the pelvis region from which we compute B_1^+ data. The size of this domain can be chosen as large as desired, but the computational costs will increase with larger data domains. Furthermore, we use 16 z-directed short dipoles uniformly positioned on a circle, with a radius of 0.2 meters, that is situated around the center of the
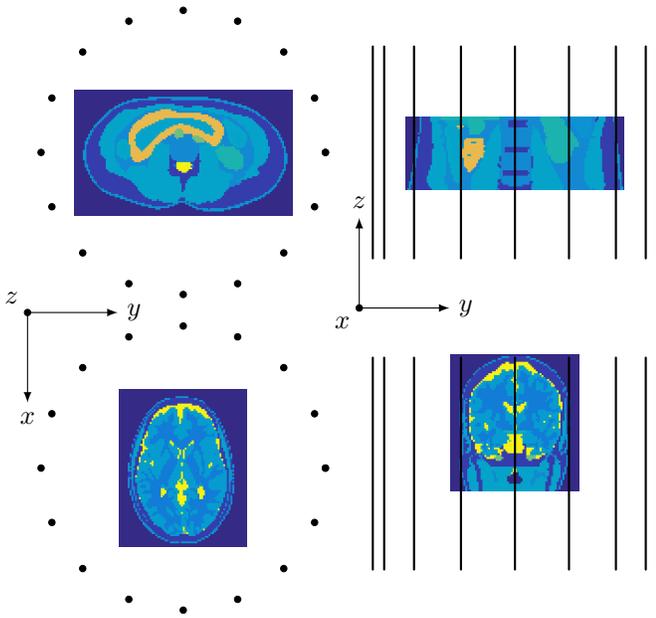
Fig. 1. Representation of the antenna positions around the objects of the two studied configurations. Transversal (left) and coronal view (right). The rectangular box is the object domain $\mathbb{D}^{\text{obj}}$, the dots and lines represent the dipoles.
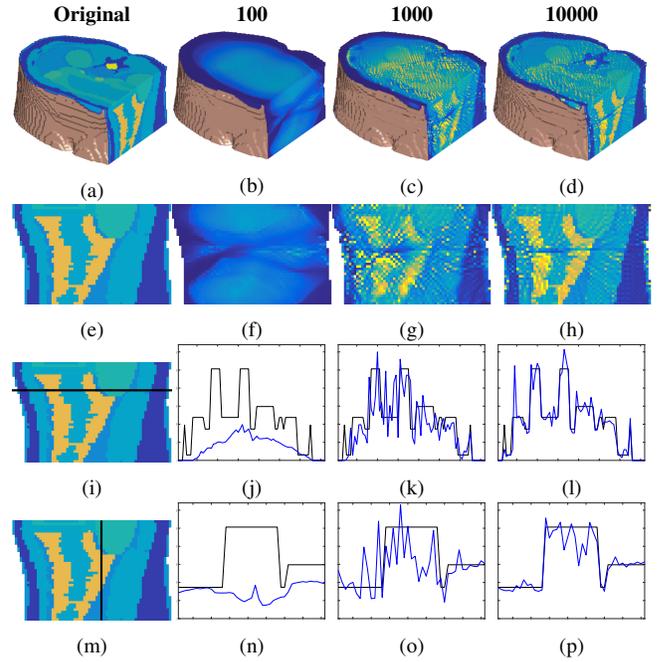

Fig. 2. Different representations of the three-dimensional reconstruction results of the abdominal region of Ella at different number of iterations. Original contrast (first column), reconstruction after 100 iterations (second column), after 1000 iterations (third column), and after 10000 iterations (last column). (j)-(l) show the magnitude of the contrast along the line indicated in (i), while (n)-(p) show the magnitude along the line indicated in (m).

object. The dipoles are 0.3 meters long, infinitely thin, have a trapezoidal current distribution, and operate in quadrature (circularly polarized) mode driven at 128 MHz (corresponding to the operating frequency of a 3T MRI system). The centers of the dipoles are positioned next to the transverse midplane of the domain of interest as shown in the top row of Fig. 1. With this dipole arrangement, we aim to mimic the integrated body coil of a 3T MR system, while at the same time such a setup allows for an easy comparison with 2D reconstruction and for flexible driving conditions. We stress that our 3D CSI-EPT method is not restricted to this chosen setup and other antenna configurations can be implemented as well.

To obtain the initial contrast source and contrast function, we start the CSI-EPT reconstruction with the backprojection procedure as described in Section III, followed by the computation of the contrast source via (8) and the electric field again via (19), since this improves the reconstruction results at the first few iterations. Furthermore, during the reconstruction we take *a priori* information into account as well. Specifically, since the position of the body is known, we set the contrast function to zero outside its support at every iteration. Moreover, during the reconstructions we set the minimum conductivity and relative permittivity to 0 and 1, respectively, and the maxima slightly higher than the values that can be found in the body part of interest.

Fig. 2 compares the actual female contrast model with the reconstruction of the contrast function at different iteration counts. The first row of Fig. 2 shows a section of the 3D reconstruction, cut off for illustration purposes at sagittal plane position 36 of 124. We observe that increasing the number of iterations results in a closer agreement with the actual model. Moreover, we observe that more iterations are required to retrieve the tissue maps of the center slices than for slices

further away from the center.

The second row shows the sagittal plane from the top row. From these subfigures we can more clearly observe the difference in reconstruction accuracy of the different slices. It shows that there are large deviations from the actual model around the center slices, while the reconstruction is more accurate in slices away from the transverse midplane. The third and fourth rows show the reconstruction values over a single horizontal and vertical line in the sagittal plane, respectively, again after a different number of iterations. In the third row we observe that the reconstruction results improve when the number of iterations is increased and that the reconstruction is very accurate at edges and at transitions between different tissue interfaces. In the fourth row we observe similar results again, however, with a large deviation around the center slice.

From the above reconstruction results we observe that, given our antenna setup, the tissue maps of the center slices are difficult to retrieve and require the largest number of CSI-EPT iterations. To investigate this issue further, we show the magnitude of the original contrast function (Fig. 3a) and the magnitude of its reconstruction after 10000 iterations (Fig. 3b) in the coronal plane at the center of the object, along with the absolute error (Fig. 3d). Also shown is the magnitude of the electric field (Fig. 3f). These figures illustrate the correspondence between the magnitude of the electric field and the quality of the contrast reconstructions in the coronal plane throughout the center of the object. The error in the reconstruction is the largest at the center in the longitudinal direction, which corresponds to locations with low $|\mathbf{E}|$.

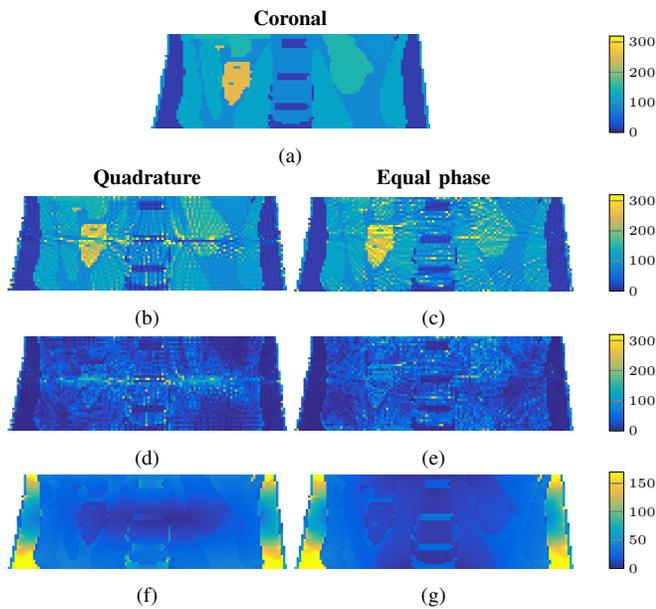To further illustrate the influence of the electric field on the

Fig. 3. Magnitude of the contrast of the model (a), the reconstruction after 10000 iterations (b,c), the corresponding absolute error (d,e) and the magnitude of the electric field strength (f,g) in the coronal plane at the center of the object with the sources operating in quadrature (left column) and operating with equal phase (right column).
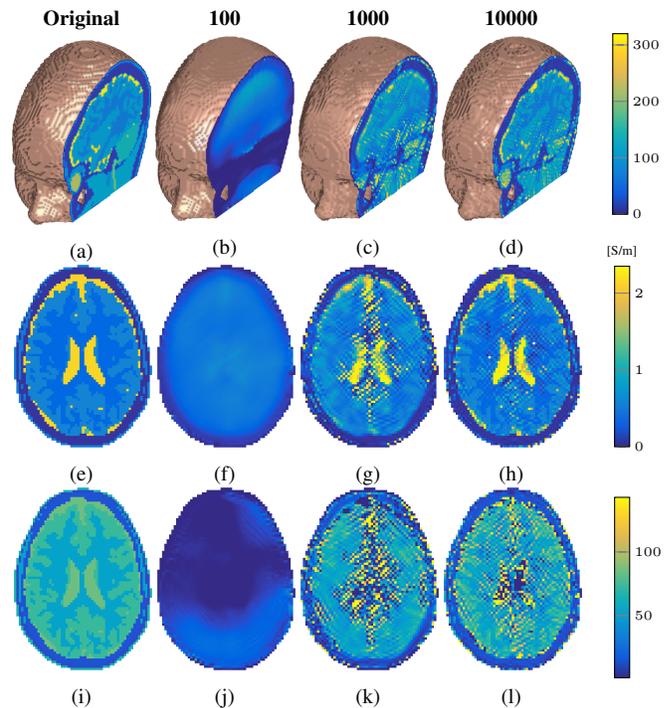

Fig. 4. Reconstruction of the conductivity and relative permittivity maps of the Ella head model. The top row shows a section of the three-dimensional representation of the magnitude of the contrast, and the second and third row show the corresponding conductivity and relative permittivity maps of slice 45, respectively. The original contrast is shown in the first column, the CSI-EPT reconstructions after 100 iterations in the second column, reconstructions after 1000 iterations in the third column, and reconstructions after 10000 iterations in the fourth column.

reconstruction, we change the antenna settings by removing the phase shift between the sources. The sources no longer operate in quadrature mode and have an equal phase. This adjustment eliminates the low electric field strength in the transverse midplane as shown in Fig. 3g and its effect on the reconstruction is shown in Fig. 3b. From Fig. 3e we observe that equal phase excitation improves the reconstruction around the center, however, at the cost of a slight degradation of the reconstruction at slices away from the transverse midplane.

In our second numerical experiment we select an object domain of 87-by-71-by-73 voxels containing the upper part of the head of the Ella body model, which is strongly inhomogeneous and has many small tissue interfaces. In this configuration we place the center of the dipoles at the lower end of the object domain, next to the nose (see Fig. 1). Fig. 4 shows a 3D visualization of a section of the contrast reconstructions obtained after 100, 1000, and 10000 CSI-EPT iterations, together with the conductivity and relative permittivity maps of slice 45 (at the higher end of the object domain) of a total of 73 slices. The 3D representation of the reconstruction of the head of Ella after 100 iterations clearly shows that the slices behind the eyes and nose are the most difficult to reconstruct, again corresponding to low electric field (not shown). Note that the air in the nasal cavity gives no B_1^+ data and therefore leaves a gap in the 3D visualization. After 1000 iterations, we observe that the tissue structures become visible in the reconstruction of the contrast function. Extracting the dielectric tissue maps from the reconstructed contrast function provides us with a fairly good reconstruction of the conductivity profile, while the relative permittivity profile is of a lower quality. Increasing the number of iterations to 10000, however, we obtain a good overall agreement with the true model, in which the small tissue transitions are clearly

visible. Furthermore, we observe from Fig. 4h and Fig. 4l that the quality of the conductivity reconstruction is higher than the quality of the relative permittivity reconstruction, which might be due to a larger influence of the conduction current ($\sigma\mathbf{E}$) to the B_1^+ field than the displacement current ($j\omega\varepsilon\mathbf{E}$) at 3T.

Finally, in the third experiment we return to the first experimental setup with the transmit antennas operating in quadrature mode. We compare reconstruction results of a single slice obtained with 3D CSI-EPT with reconstruction results obtained via the 2D CSI-EPT algorithm of [19]. For the 3D algorithm, we shift the object domain, such that the transversal slice is 4.5 cm away from the transversal midplane. For the 2D algorithm, we increase the object domain with 15 cm on the top and bottom of the model, and we simulate 3D B_1^+ data in the transverse midplane, which we use together with 2D incident fields for the reconstructions. The original profile is shown in Fig. 5a, the reconstruction result of this slice with 3D CSI-EPT after 10000 iterations is shown in Fig. 5b and the 2D CSI-EPT reconstruction result obtained after 1000 iterations is shown in Fig. 5c. The 2D reconstruction shows large artifacts at the center and also at tissue transitions, especially at the outer edge. Since the 2D algorithm assumes that the sources and object are invariant in the longitudinal direction, we first replace all slices of the object in this longitudinal direction by the transverse midplane. By simulating B_1^+ data in the midplane of the resulting
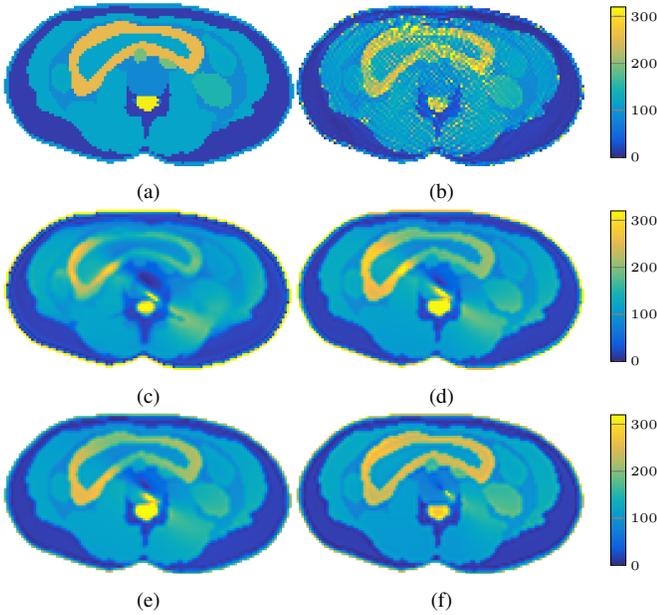
Fig. 5. Illustration of the shortcomings of a 2D reconstruction based on 3D B_1^+ data due to longitudinal invariance assumptions. The magnitude of the original contrast of the transverse midplane (a), the reconstruction of the same slice with 3D CSI-EPT after 10000 iterations with the slice away from the midplane (b) and the reconstruction with 2D CSI-EPT after 1000 iterations using the B_1^+ field of the transverse midplane (c). Furthermore, the results after increasing the longitudinal invariance in the model step-by-step by first making the object homogeneous in the longitudinal direction (d), second by applying a uniform current distribution on the sources (e), and third by changing the length of the object from 40 to 80 cm (f).

cylindrical object and using this data as input for 2D CSI-EPT, we obtain the reconstruction result shown in Fig. 5d, which slightly improves the reconstruction. A further improvement is observed if the currents in the z-direction are also set to be uniform (Fig. 5e), and reconstructions improve even further if we increase the voxel length in the z-direction from 2.5 mm to 5 mm (Fig. 5f). We stress that Fig. 5c is obtained by applying 2D CSI-EPT on 3D data, while Figs. 5d-f are only included to demonstrate that the 2D CSI-EPT reconstructions improve as the complete configuration approaches an idealized 2D implementation. From these experiments we conclude that 2D CSI-EPT is appropriate under very specific conditions only, while 3D CSI EPT is not based on any invariance assumptions and generally applicable.

V. DISCUSSION AND CONCLUSION

In this paper we have presented a proof of principle of three-dimensional CSI-EPT. The method takes the volumetric integral representations for the RF field as a starting point and is able to successfully reconstruct strongly inhomogeneous 3D tissue profiles based on B_1^+ data collected within the domain of interest. The method does not rely on any particular field structure and, as opposed to the two-dimensional implementation presented in [19], invariance in the longitudinal direction is not assumed. However, the current 3D method is computationally much more intensive than its 2D counterpart, since full 3D structures are inverted based on volumetric B_1^+ data. Moreover, the number of iterations required to arrive

at a reconstruction of sufficient quality is generally fairly large, which is characteristic for gradient methods such as CSI-EPT. Typical run times of a Matlab implementation of 3D CSI-EPT take several hours for large voxel sizes, while the computation times increases for more refined models. For example, 10000 iterations of the fine-scaled head model of Fig. 4 requires around 11 hours on a standard laptop or pc. Future work will therefore focus on preconditioning techniques that reduce the number of CSI iterations without significantly increasing the total computational costs. Including *a priori* information through constraints or using this information to construct an improved initial guess will also be investigated. Reconstructions obtained from other EPT methods (such as the direct EPT method from Haacke [6]) can be used as an initial guess for CSI-EPT as well.

Our reconstruction results indicate that accurate conductivity and relative permittivity reconstructions are most difficult to obtain in regions where the magnitude of the electric field is relatively low. The normalized root-mean-square error of the dielectric reconstructions (normalized over the range of the dielectric properties), corresponding to the 25% of voxels with the lowest up to the 25% of voxels with the highest electric field magnitude in quadrature setting inside the object corresponding to Fig. 3, are 0.23, 0.13, 0.10 and 0.06 for the conductivity and 0.39, 0.25, 0.20 and 0.10 for the relative permittivity reconstruction, respectively. Similar results were obtained for 2D CSI-EPT in [19], and it shows similarities with the problem of low convection field discussed in [14], which corresponds to regions with low conduction and displacement current. Low electric fields amplitudes result in low induced electric currents and the impact of these currents on the total B_1^+ field is small. Our CSI-EPT reconstruction technique therefore requires many iterations to reconstruct the dielectric tissue maps of regions with a low E-field amplitude. Removing the phase shift between the sources, even though this is not a realistic setting in practice due to nulling of the magnetic field, clearly shows the influence of the antenna settings and the electric field strength on the reconstructions again indicating that the magnitude of the electric field strength should be sufficiently large to readily reconstruct the local dielectric tissue maps. Reconstructions in low E-field regions can be improved by incorporating complementary antenna settings or through active or passive shimming [19], [29].

In this paper, we have assumed noiseless B_1^+ data. In a real experiment, however, the amplitude and phase of the B_1^+ field are measured separately and each is contaminated by noise and other perturbations in the data. To take perturbations due to noise into account, noise suppression techniques such as total variation can be included [19], [30]. Moreover, in phase measurements, only the transceive phase can be measured, which is the superposition of the phase of the B_1^+ field and the phase of the B_1^- field. To obtain an estimate of the B_1^+ phase, the transceive phase approximation can be implemented [4], [5]. However, this approximation does not always produce an accurate B_1^+ phase and leads to reconstruction artifacts [31]. In future work we will therefore also focus on handling transceive phase along with total variation noise suppression techniques.

Finally, we address the fact that the iterative method requires

the incident field to be known. In this work we considered this field to be determined solely by the known coil geometry. In practice, the loading from a human subject inside the RF coil slightly influences the incident, and thus the scattered and total fields. Any difference between the modeled and actual applied incident field will result in distortion in the reconstructed EP maps. An extreme example of the effects of an incorrect incident field is shown in [20]. The loading effect on the incident field can easily be estimated from more thorough simulations, such as finite-difference time-domain methods, based on a few different loading conditions. In this paper, we presented a dipole antenna configuration, but other antenna arrangements can also be implemented, such as the in-built birdcage body coil that is used on practically every MRI system. In practice, one would use the antenna configuration that resembles the actual setup as closely as possible.

APPENDIX

The spatial discretization of the integral representations for the RF field closely follows [32] except that here we present the discretized equations in Kronecker product form to obtain global discretized representations for the fields.

We start by extending the object domain to a rectangular computational domain $\mathbb{D}^{\mathrm{comp}}$ with side lengths $\ell_i > 0$, $i = x, y, z$, such that $\mathbb{D}^{\mathrm{obj}} \subseteq \mathbb{D}^{\mathrm{comp}}$. This can always be achieved, since the contrast function vanishes outside the object domain $\mathbb{D}^{\mathrm{obj}}$. Subsequently, the computational domain is subdivided into nonoverlapping discretization cells

$$
\begin{aligned}
\mathbb{D}^{pqr} = \{ & p\delta_x < x < (p+1)\,\delta_x, \\
& q\delta_y < y < (q+1)\,\delta_y, \\
& r\delta_z < z < (r+1)\,\delta_z \},
\end{aligned} \tag{22}
$$

for $p = 0, 1, \ldots, P+1$, $q = 0, 1, \ldots, Q+1$, and $r = 0, 1, \ldots, R+1$, where $P \geq 1$, $Q \geq 1$, and $R \geq 1$ are integers. Cells with an index $p = 0$, $p = P+1$, $q = 0$, $q = Q+1$, $r = 0$, or $r = R+1$ are referred to as boundary cells, while all other cells are called interior cells. Obviously, the side lengths of a discretization cell are given by

$$
\delta_x = \frac{l_x}{P+2}, \quad \delta_y = \frac{l_y}{Q+2}, \quad \text{and} \quad \delta_z = \frac{l_z}{R+2}, \tag{23}
$$

and the position vector of the midpoint of a discretization cell is given by

$$
\mathbf{x}_{pqr} = x_p \mathbf{i}_x + y_q \mathbf{i}_y + z_r \mathbf{i}_z, \tag{24}
$$

with

$$
x_p = \frac{\delta_x}{2} + p\delta_x \quad \text{for} \quad p = 0, 1, \ldots, P+1, \tag{25}
$$

$$
y_q = \frac{\delta_y}{2} + q\delta_y \quad \text{for} \quad q = 0, 1, \ldots, Q+1, \tag{26}
$$

and

$$
z_r = \frac{\delta_z}{2} + r\delta_z \quad \text{for} \quad r = 0, 1, \ldots, R+1. \tag{27}
$$

Note that the total number of discretization cells is $(P+2)\,(Q+2)\,(R+2)$.

Having introduced our computational grid, we now discretize the integral representations of (2) and (3). Using the

definition of the scattered field and writing these equations out in components, we have

$$
E_x = E_x^{\mathrm{inc}} + k_{\mathsf{b}}^2 A_x + \partial_x^2 A_x + \partial_x \partial_y A_y + \partial_x \partial_z A_z, \tag{28}
$$

$$
E_y = E_y^{\mathrm{inc}} + k_{\mathsf{b}}^2 A_y + \partial_y \partial_x A_x + \partial_y^2 A_y + \partial_y \partial_z A_z, \tag{29}
$$

$$
E_z = E_z^{\mathrm{inc}} + k_{\mathsf{b}}^2 A_z + \partial_z \partial_x A_x + \partial_z \partial_y A_y + \partial_z^2 A_z, \tag{30}
$$

and

$$
H_x = H_x^{\mathrm{inc}} + \eta_{\mathsf{b}} \left(\partial_y A_z - \partial_z A_y \right), \tag{31}
$$

$$
H_y = H_y^{\mathrm{inc}} + \eta_{\mathsf{b}} \left(\partial_z A_x - \partial_x A_z \right), \tag{32}
$$

$$
H_z = H_z^{\mathrm{inc}} + \eta_{\mathsf{b}} \left(\partial_x A_y - \partial_y A_x \right). \tag{33}
$$

We only discuss the discretization of (28), since all other equations can be handled in a similar manner.

As a first step, we require that (28) holds at the midpoints of the inner discretization cells, that is, for $\mathbf{x} = \mathbf{x}_{pqr}$ with $p = 1, 2, \ldots, P$, $q = 1, 2, \ldots, Q$, and $r = 1, 2, \ldots, R$. In other words, we require that

$$
\begin{aligned}
E_x\left(\mathbf{x}_{pqr}\right) = {} & E_x^{\mathrm{inc}}(\mathbf{x}_{pqr}) + k_{\mathsf{b}}^2 A_x(\mathbf{x}_{pqr}) \\
& + \left. \partial_x^2 A_x \right|_{\substack{x=x_p \\ y=y_q \\ z=z_r}} + \left. \partial_x \partial_y A_y \right|_{\substack{x=x_p \\ y=y_q \\ z=z_r}} \\
& + \left. \partial_x \partial_z A_z \right|_{\substack{x=x_p \\ y=y_q \\ z=z_r}},
\end{aligned} \tag{34}
$$

for $p = 1, 2, \ldots, P$, $q = 1, 2, \ldots, Q$, and $r = 1, 2, \ldots, R$. Second, we follow [32] and approximate the spatial derivatives by second-order central finite-difference formulas. To implement these formulas using Kronecker products, we introduce the first-order differentiation matrix with respect to the x-coordinate as

$$
\mathsf{X} = \frac{1}{2\delta_x}
\begin{bmatrix}
-1 & 0 & 1 & & \\
& -1 & 0 & 1 & \\
& & \ddots & \ddots & \ddots \\
& & & -1 & 0 & 1
\end{bmatrix}, \tag{35}
$$

where the elements that are not shown are zero. First-order differentiation matrices Y and Z with respect to the y- and z-coordinate are defined in a similar manner, but with δ_x replaced by δ_y and δ_z, respectively. Furthermore, second-order differentiation matrices are introduced as

$$
\mathsf{L}_i = \frac{1}{(\delta_i)^2}
\begin{bmatrix}
1 & -2 & 1 & & \\
& 1 & -2 & 1 & \\
& & \ddots & \ddots & \ddots \\
& & & 1 & -2 & 1
\end{bmatrix}, \tag{36}
$$

for $i = x, y, z$. The matrices L_x and X are P-by-$(P+2)$, L_y and Y are Q-by-$(Q+2)$, and L_z and Z are R-by-$(R+2)$. Note that larger or filter kernels could also be introduced, for example for noisy data [4]. Subsequently, for each slice in the z-direction we introduce a $(P+2)$-by-$(Q+2)$ matrix $\mathsf{A}_x^{[r]}$ with elements given by

$$
\left(\mathsf{A}_x^{[r]} \right)_{pq} = A_x\left(x_p, y_q, z_r\right), \quad r = 0, 1, \ldots, R+1. \tag{37}
$$

The above formula defines a collection of $R+2$ matrices $\mathsf{A}_x^{[0]}$, $\mathsf{A}_x^{[1]}$, ..., $\mathsf{A}_x^{[R+1]}$ containing the x-component of the vector potential at the midpoints of all discretization cells. These matrices can be turned into vectors by stacking their columns from left to right using the vec-operation [33]. We write

$$\mathsf{a}_x^{[r]} = \text{vec}\left(\mathsf{A}_x^{[r]}\right), \tag{38}$$

for $r = 0, 1, \ldots, R + 1$. Matrices and vectors for the y- and z-components of the vector potential as well as for all components of the electric field strength are defined similarly. Finally, we introduce the restriction operators in each Cartesian direction as

$$\mathsf{R}_k = \begin{bmatrix} 0 & \mathsf{I}_k & 0 \end{bmatrix}, \quad k = P, Q, R, \tag{39}$$

of sizes P-by-$(P + 2)$, Q-by-$(Q + 2)$, and R-by-$(R + 2)$ for R_P, R_Q, and R_R, respectively and with I_k the identity operator of order k.

Having introduced all these matrices, the discretized form of (34) can be written for every slice $r = 1, 2, \ldots, R$ in the z-direction as

$$\begin{aligned}
\mathsf{R}_P\mathsf{E}_x^{[r]}\mathsf{R}_Q^\mathsf{T} = {} & \mathsf{R}_P\mathsf{E}_x^{\text{inc};[r]}\mathsf{R}_Q^\mathsf{T} + k_\mathsf{b}^2\mathsf{R}_P\mathsf{A}_x^{[r]}\mathsf{R}_Q^\mathsf{T} \\
& + \mathsf{L}_x\mathsf{A}_x^{[r]}\mathsf{R}_Q^\mathsf{T} + \mathsf{X}\mathsf{A}_y^{[r]}\mathsf{Y}^\mathsf{T} \\
& + \left[\frac{1}{2\delta_z}\mathsf{X}\mathsf{A}_z^{[r+1]}\mathsf{R}_Q^\mathsf{T} - \frac{1}{2\delta_z}\mathsf{X}\mathsf{A}_z^{[r-1]}\mathsf{R}_Q^\mathsf{T}\right].
\end{aligned} \tag{40}$$

Applying the vec-operation to this equation, using the linearity of this operator, and the property [33]

$$\text{vec}\left(\mathsf{A}\mathsf{X}\mathsf{B}^\mathsf{T}\right) = (\mathsf{B} \otimes \mathsf{A})\,\text{vec}\,(\mathsf{X}), \tag{41}$$

where $\otimes$ denotes the Kronecker product, we obtain

$$\begin{aligned}
(\mathsf{R}_Q \otimes \mathsf{R}_P)\mathsf{e}_x^{[r]} = {} & (\mathsf{R}_Q \otimes \mathsf{R}_P)\mathsf{e}_x^{\text{inc};[r]} + k_\mathsf{b}^2(\mathsf{R}_Q \otimes \mathsf{R}_P)\mathsf{a}_x^{[r]} \\
& + (\mathsf{R}_Q \otimes \mathsf{L}_x)\mathsf{a}_x^{[r]} + (\mathsf{Y} \otimes \mathsf{X})\mathsf{a}_y^{[r]} \\
& + \left[\frac{1}{2\delta_z}(\mathsf{R}_Q \otimes \mathsf{X})\mathsf{a}_z^{[r+1]} - \frac{1}{2\delta_z}(\mathsf{R}_Q \otimes \mathsf{X})\mathsf{a}_z^{[r-1]}\right],
\end{aligned} \tag{42}$$

for $r = 1, 2, \ldots, R$. Finally, we stack the vectors $\mathsf{a}_x^{[0]}$, $\mathsf{a}_x^{[1]}$, ..., $\mathsf{a}_x^{[R+1]}$ of all slices in one large total vector for the x-component of the vector potential. This defines the $(P + 2)(Q + 2)(R + 2)$-by-1 vector

$$\mathsf{a}_x = \left[\left(\mathsf{a}_x^{[0]}\right)^\mathsf{T}, \left(\mathsf{a}_x^{[1]}\right)^\mathsf{T}, \ldots, \left(\mathsf{a}_x^{[R+1]}\right)^\mathsf{T}\right]^\mathsf{T} \tag{43}$$

and total vectors for the y- and z-components of the vector potential and all components of the electric field strength are defined similarly. With the introduction of these total vectors and using the properties of the Kronecker product, the R equations of (42) can be written as a single global equation

$$\begin{aligned}
\tilde{\mathsf{I}}\mathsf{e}_x = {} & \tilde{\mathsf{I}}\mathsf{e}_x^{\text{inc}} + k_\mathsf{b}^2\tilde{\mathsf{I}}\mathsf{a}_x \\
& + (\mathsf{R}_R \otimes \mathsf{R}_Q \otimes \mathsf{L}_x)\mathsf{a}_x + (\mathsf{R}_R \otimes \mathsf{Y} \otimes \mathsf{X})\mathsf{a}_y \\
& + (\mathsf{Z} \otimes \mathsf{R}_Q \otimes \mathsf{X})\mathsf{a}_z,
\end{aligned} \tag{44}$$

with $\tilde{\mathsf{I}} = (\mathsf{R}_R \otimes \mathsf{R}_Q \otimes \mathsf{R}_P)$. Notice that the sparse restriction matrices R_k, $k = P, Q, R$, and the sparse differentiation matrices X, Y, Z, and L_i, $i = x, y, z$ are easily implemented

in any programming language, while the Kronecker products can be carried out using any Kronecker product routine such as the kron command in Matlab. Finally, we note that the global discretized equation (44) is similar in form as its continuous counterpart as given by (28).

A. Weakened vector potential

The final step in our discretization procedure consists of relating the vector potential to the electric field strength at the midpoints of the discretization cells. Recall that in a continuous setting this relation is given by (4). With $\mathbf{x} \in \mathbb{D}^{\text{obj}}$, the Green's function is singular when $\mathbf{x}' = \mathbf{x}$, which may lead to difficulties when discretizing the integral on a computational grid. To circumvent this problem, we follow [34] and replace the Green's function by the weakened Green's function G^w that satisfies the equation

$$(\nabla^2 + k_\mathsf{b}^2)G^\text{w} = -f(\mathbf{x}), \tag{45}$$

where

$$f(\mathbf{x}) = \begin{cases} \frac{3}{4\pi a^3}, & \text{if } \mathbf{x} \in \mathbb{D}^{\text{ball}}, \\ 0, & \text{if } \mathbf{x} \notin \mathbb{D}^{\text{ball}}, \end{cases} \tag{46}$$

with $\mathbb{D}^{\text{ball}}$ a ball of radius $a = \min\{\delta_x, \delta_y, \delta_z\}/2$ centered at the origin. In addition to (45), G^w is required to satisfy the Sommerfeld radiation condition [35].

The weakened Green's function can be computed explicitly for $\mathbf{x} \neq \mathbf{0}$ as

$$G^\text{w}(\mathbf{x}) = \frac{\exp(-\mathrm{j}k_\mathsf{b}\,|\mathbf{x}|)}{4\pi|\mathbf{x}|}\frac{3}{(k_\mathsf{b}a)^2}\left[\frac{\sin(k_\mathsf{b}a)}{k_\mathsf{b}a} - \cos(k_\mathsf{b}a)\right], \tag{47}$$

and for $\mathbf{x} = \mathbf{0}$ as [34]

$$G^\text{w}(\mathbf{0}) = \frac{3}{4\pi k_\mathsf{b}^2 a^3}\left[(1 + \mathrm{j}k_\mathsf{b}a)\exp(-\mathrm{j}k_\mathsf{b}a) - 1\right]. \tag{48}$$

Note that

$$G^\text{w}(\mathbf{x}) = G(\mathbf{x})\left\{1 + O[(k_\mathsf{b}a)^2]\right\} \quad \text{for } \mathbf{x} \neq \mathbf{0} \text{ as } k_\mathsf{b}a \downarrow 0, \tag{49}$$

showing that with the particular choice for the radius a, the weakening procedure is consistent with the second-order accurate finite-difference approximations for the spatial derivatives.

Replacing the Green's function in the expression for the vector potential by its weak form, we arrive at the weakened vector potential

$$\mathbf{A}^\text{w}(\mathbf{x}) = \int_{\mathbf{x}' \in \mathbb{D}^{\text{obj}}} G^\text{w}(\mathbf{x} - \mathbf{x}')\chi(\mathbf{x}')\mathbf{E}(\mathbf{x}')\,\mathrm{d}V \tag{50}$$

and if we assume that the contrast function is constant within each discretization cell, that is, $\chi(\mathbf{x}) = \chi_{pqr}$ if $\mathbf{x} \in \mathbb{D}^{pqr}$, then we can write

$$\mathbf{A}^\text{w}(\mathbf{x}) = \sum_{p=0}^{P+1}\sum_{q=0}^{Q+1}\sum_{r=0}^{R+1}\chi_{pqr}\int_{\mathbf{x}' \in \mathbb{D}^{pqr}} G^\text{w}(\mathbf{x} - \mathbf{x}')\mathbf{E}(\mathbf{x}')\,\mathrm{d}V. \tag{51}$$

Finally, the remaining integral can be approximated by the midpoint rule, which results in

$$\mathbf{A}^\text{w}(\mathbf{x}) \approx \delta_x\delta_y\delta_z\sum_{p=0}^{P+1}\sum_{q=0}^{Q+1}\sum_{r=0}^{R+1}\chi_{pqr}G^\text{w}(\mathbf{x} - \mathbf{x}_{pqr})\mathbf{E}(\mathbf{x}_{pqr}) \tag{52}$$

and since the vector potential is required at the midpoints $\mathbf{x}_{ijk}$, we arrive at

$$\mathbf{A}^{\mathrm{w}}(\mathbf{x}_{ijk})$$
$$= \delta_x \delta_y \delta_z \sum_{p=0}^{P+1} \sum_{q=0}^{Q+1} \sum_{r=0}^{R+1} G^{\mathrm{w}}(\mathbf{x}_{ijk} - \mathbf{x}_{pqr}) \chi_{pqr} \mathbf{E}(\mathbf{x}_{pqr}), \quad (53)$$

for $i = 0, 1, \ldots, P+1$, $j = 0, 1, \ldots, Q+1$ and $k = 0, 1, \ldots, R+1$. Storing the vector potential and electric field strength approximations in the previously introduced vectors a_i and e_i, $i = x, y, z$, we arrive at the discretized counterpart of the weakened vector potential

$$\mathsf{a}_i = \mathsf{GCe}_i, \quad i = x, y, z, \quad (54)$$

where G is a square matrix of order $(P+2)(Q+2)(R+2)$ representing the summations with the weakened Green's function in (53) including multiplication by $\delta_x \delta_y \delta_z$ and C is a diagonal matrix with the contrast values of the discretization cells on its diagonal. Finally, we note that the electric field strength approximations are defined on interior discretization cells only (note the range of the indices in (34)), while the vectors e_i contain elements corresponding to boundary cells as well. These elements are included so that the vectors a_i and e_i have the same number of elements and the action of matrix G on a vector can be computed using the Fast Fourier Transform (FFT).

Putting everything together, we arrive at the discretized counterpart of (28) as

$$\tilde{\mathsf{I}}\mathsf{e}_x = \tilde{\mathsf{I}}\mathsf{e}_x^{\mathrm{inc}} + k_{\mathsf{b}}^2 \tilde{\mathsf{I}}\mathsf{GCe}_x$$
$$+ (\mathsf{R}_R \otimes \mathsf{R}_Q \otimes \mathsf{L}_x)\mathsf{GCe}_x + (\mathsf{R}_R \otimes \mathsf{Y} \otimes \mathsf{X})\mathsf{GCe}_y \quad (55)$$
$$+ (\mathsf{Z} \otimes \mathsf{R}_Q \otimes \mathsf{X})\mathsf{GCe}_z.$$

Equations (29) and (30) can be discretized in a similar manner and combining the resulting discretized equations with (55), the discretized counterpart of the object operator can be identified as

$$\mathsf{G}_{\mathrm{obj}} = \left[k_{\mathsf{b}}^2 \left(\mathsf{I}_3 \otimes \tilde{\mathsf{I}} \right) + \mathsf{D} \right] (\mathsf{I}_3 \otimes \mathsf{G}), \quad (56)$$

where D is the discretized gradient-divergence operator given by

$$\mathsf{D} = \begin{pmatrix} \mathsf{R}_R \otimes \mathsf{R}_Q \otimes \mathsf{L}_x & \mathsf{R}_R \otimes \mathsf{Y} \otimes \mathsf{X} & \mathsf{Z} \otimes \mathsf{R}_Q \otimes \mathsf{X} \\ \mathsf{R}_R \otimes \mathsf{Y} \otimes \mathsf{X} & \mathsf{R}_R \otimes \mathsf{L}_y \otimes \mathsf{R}_P & \mathsf{Z} \otimes \mathsf{Y} \otimes \mathsf{R}_P \\ \mathsf{Z} \otimes \mathsf{R}_Q \otimes \mathsf{X} & \mathsf{Z} \otimes \mathsf{Y} \otimes \mathsf{R}_P & \mathsf{L}_z \otimes \mathsf{R}_Q \otimes \mathsf{R}_P \end{pmatrix}. \quad (57)$$

The discretized counterpart of the data operator can be obtained by following similar steps as above.

REFERENCES

[1] U. Katscher, T. Voigt, C. Findeklee, P. Vernickel, K. Nehrke, and O. Doessel, "Determination of electric conductivity and local SAR via B1 mapping," *IEEE Trans. Med. Imag.*, vol. 28, no. 9, pp. 1365–1374, 2009.

[2] S.-Y. Kim, J. Shin, D.-H. Kim, M. J. Kim, E.-K. Kim, H. J. Moon, and J. H. Yoon, "Correlation between conductivity and prognostic factors in invasive breast cancer using magnetic resonance electric properties tomography (MREPT)," *Eur. Radiol.*, vol. 26, no. 7, pp. 2317–2326, 2016.

[3] E. Balidemaj, H. P. Kok, G. Schooneveldt, A. L. H. M. W. van Lier, R. F. Remis, L. J. A. Stalpers, H. Westerveld, A. J. Nederveen, C. A. T. van den Berg, and J. Crezee, "Hyperthermia treatment planning for cervical cancer patients based on electrical conductivity tissue properties acquired in vivo with EPT at 3T MRI," *Int. J. Hyperther.*, vol. 32, no. 5, pp. 558–568, 2016.

[4] U. Katscher and C. A. T. van den Berg, "Electric properties tomography: Biochemical, physical and technical background, evaluation and clinical applications," *NMR Biomed.*, vol. 30, no. 8, 2017.

[5] J. Liu, Y. Wang, U. Katscher, and B. He, "Electrical properties tomography based on B_1 maps in mri: Principles, applications, and challenges," *IEEE T Bio-med. Eng.*, vol. 64, no. 11, pp. 2515–2530, 2017.

[6] E. M. Haacke, L. S. Petropoulos, E. W. Nilges, and D. H. Wu, "Extraction of conductivity and permittivity using magnetic resonance imaging," *Phys. Med. Biol.*, vol. 36, no. 6, p. 723, 1991.

[7] H. Wen, "Noninvasive quantitative mapping of conductivity and dielectric distributions using RF wave propagation effects in high-field MRI," in *Proc. SPIE*, vol. 5030, San Diego, CA, USA, 2003, pp. 471–477.

[8] T. Voigt, U. Katscher, and O. Doessel, "Quantitative conductivity and permittivity imaging of the human brain using electric properties tomography," *Magn. Reson. Med.*, vol. 66, no. 2, pp. 456–466, 2011.

[9] A. L. H. M. W. van Lier, D. O. Brunner, K. P. Pruessmann, D. W. J. Klomp, P. R. Luijten, J. J. W. Lagendijk, and C. A. T. van den Berg, "B1+ phase mapping at 7T and its application for in vivo electrical conductivity mapping," *Magn. Reson. Med.*, vol. 67, no. 2, pp. 552–561, 2012.

[10] D. K. Sodickson, L. Alon, C. M. Deniz, R. Brown, B. Zhang, G. C. Wiggins, G. Y. Cho, N. B. Eliezer, D. S. Novikov, R. Lattanzi *et al.*, "Local maxwell tomography using transmit-receive coil arrays for contact-free mapping of tissue electrical properties and determination of absolute RF phase," in *Proc. ISMRM, Melbourne, Vic., Australia*, 2012, p. 387.

[11] X. Zhang, P.-F. van de Moortele, S. Schmitter, and B. He, "Complex B1 mapping and electrical properties imaging of the human brain using a 16-channel transceiver coil at 7T," *Magn. Reson. Med.*, vol. 69, no. 5, pp. 1285–1296, 2013.

[12] J. Liu, X. Zhang, P.-F. van de Moortele, S. Schmitter, and B. He, "Determining electrical properties based on B1 fields measured in an MR scanner using a multi-channel transmit/receive coil: a general approach," *Phys. Med. Biol.*, vol. 58, no. 13, p. 4395, 2013.

[13] J. P. Marques, D. K. Sodickson, O. Ipek, C. M. Collins, and R. Gruetter, "Single acquisition electrical property mapping based on relative coil sensitivities: a proof-of-concept demonstration," *Magn. Reson. Med.*, vol. 74, no. 1, pp. 185–195, 2015.

[14] F. S. Hafalir, O. F. Oran, N. Gurler, and Y. Z. Ider, "Convection-reaction equation based magnetic resonance electrical properties tomography (cr-MREPT)," *IEEE Trans. Med. Imag.*, vol. 33, no. 3, pp. 777–793, 2014.

[15] J. Liu, X. Zhang, S. Schmitter, P.-F. van de Moortele, and B. He, "Gradient-based electrical properties tomography (gEPT): A robust method for mapping electrical properties of biological tissues in vivo using magnetic resonance imaging," *Magn. Reson. Med.*, vol. 74, no. 3, pp. 634–646, 2015.

[16] N. Gurler and Y. Z. Ider, "Gradient-based electrical conductivity imaging using MR phase," *Magn. Reson. Med.*, vol. 77, no. 1, pp. 137–150, 2017.

[17] A. Borsic, I. Perreard, A. Mahara, and R. J. Halter, "An inverse problems approach to MR-EPT image reconstruction," *IEEE Trans. Med. Imag.*, vol. 35, no. 1, pp. 244–256, 2016.

[18] K. M. Ropella and D. C. Noll, "A regularized, model-based approach to phase-based conductivity mapping using MRI," *Magn. Reson. Med.*, vol. 78, no. 5, pp. 2011–2021, 2016.

[19] E. Balidemaj, C. A. T. van den Berg, J. Trinks, A. L. H. M. W. van Lier, A. J. Nederveen, L. J. A. Stalpers, H. Crezee, and R. F. Remis, "CSI-EPT: a contrast source inversion approach for improved MRI-based electric properties tomography," *IEEE Trans. Med. Imag.*, vol. 34, no. 9, pp. 1788–1796, 2015.

[20] A. Arduino, L. Zilberti, M. Chiampi, and O. Bottauscio, "CSI-EPT in presence of RF-shield for MR-coils," *IEEE Trans. Med. Imag.*, vol. 36, no. 7, pp. 1396–1404, 2017.

[21] E. Balidemaj, C. A. T. van den Berg, A. L. H. M. W. van Lier, A. J. Nederveen, L. J. A. Stalpers, H. Crezee, and R. F. Remis, "B1-based SAR reconstruction using contrast source inversion–electric properties

tomography (CSI-EPT)," *Med. Biol. Eng. Comput.*, vol. 55, no. 2, pp. 225–233, 2017.

[22] R. Hong, S. Li, J. Zhang, Y. Zhang, N. Liu, Z. Yu, and Q. H. Liu, "3-D MRI-based electrical properties tomography using the volume integral equation method," *IEEE T. Microw. Theory*, vol. 65, no. 12, pp. 4802–4811, 2017.

[23] A. T. Hoop, *Handbook of radiation and scattering of waves*. London: Academic press, 1995.

[24] P. M. Van den Berg and A. Abubakar, "Contrast source inversion method: State of art," *Progress in Electromagnetics Research*, vol. 34, no. 11, pp. 189–218, 2001.

[25] P. M. van den Berg and R. E. Kleinman, "A contrast source inversion method," *Inverse Probl.*, vol. 13, no. 6, p. 1607, 1997.

[26] P. M. van den Berg, A. L. Van Broekhoven, and A. Abubakar, "Extended contrast source inversion," *Inverse Probl.*, vol. 15, no. 5, p. 1325, 1999.

[27] E. K. P. Chong and S. H. Zak, *An introduction to optimization*. John Wiley & Sons, 2013, vol. 76.

[28] A. Christ, W. Kainz, E. G. Hahn, K. Honegger, M. Zefferer, E. Neufeld, W. Rascher, R. Janka, W. Bautz, J. Chen *et al.*, "The virtual family development of surface-based anatomical models of two adults and two children for dosimetric simulations," *Phys. Med. Biol.*, vol. 55, no. 2, pp. 23–38, 2010.

[29] R. Schmidt and A. Webb, "A new approach for electrical properties estimation using a global integral equation and improvements using high permittivity materials," *J. Magn. Reson.*, vol. 262, pp. 8–14, 2016.

[30] P. M. van den Berg and R. E. Kleinman, "A total variation enhanced modified gradient algorithm for profile reconstruction," *Inverse Probl.*, vol. 11, no. 3, p. L5, 1995.

[31] A. L. H. M. W. van Lier, A. Raaijmakers, T. Voigt, J. J. W. Lagendijk, P. R. Luijten, U. Katscher, and C. A. T. Berg, "Electrical properties tomography in the human brain at 1.5, 3, and 7T: a comparison study," *Magn. Reson. Med.*, vol. 71, no. 1, pp. 354–363, 2014.

[32] A. Abubakar and P. M. van den Berg, "Three-dimensional inverse scattering applied to cross-well induction sensors," *IEEE T. Geosci. Remote*, vol. 38, no. 4, pp. 1669–1681, 2000.

[33] R. A. Horn and C. R. Johnson, *Topics in Matrix Analysis*. Cambridge: Cambridge university press, 2010.

[34] P. Zwamborn and P. M. van den Berg, "The three dimensional weak form of the conjugate gradient FFT method for solving scattering problems," *IEEE T. Microw. Theory*, vol. 40, no. 9, pp. 1757–1766, 1992.

[35] J. G. Van Bladel, *Electromagnetic fields*, 2nd ed. Hoboken, NJ, USA: John Wiley & Sons, 2007, vol. 19.